Probabilistic permanent fault displacement hazard via Monte Carlo simulation and its consideration for the probabilistic risk assessment of buried continuous steel pipelines

Yin Cheng[†] and Sinan Akkar[†,1]

[†]*Earthquake Engineering Department, Kandilli Observatory and Earthquake Research Institute, Boğaziçi University 34684 İstanbul, Turkey*

SUMMARY

Permanent fault displacements (PFDs) due to fault ruptures emerging at the surface are critical for seismic design and risk assessment of continuous pipelines because they impose significant compressive and tensile strains at pipe-fault crossings. The complexity of fault rupture, inaccurate mapping of fault location and uncertainties in fault-pipe crossing geometries require probabilistic approaches for assessing the PFD hazard and mitigating pipeline failure risk against PFD. The probabilistic approaches are currently waived in seismic design of pipelines. Bearing on these facts, this paper first assesses the probabilistic PFD hazard by using Monte Carlo based stochastic simulations whose theory and implementation are given in detail. The computed hazard is then used in the probabilistic risk assessment approach to calculate the failure probability of continuous pipelines under different PFD levels as well as pipe cross-section properties. Our probabilistic pipeline risk computations take into account uncertainties arising from complex fault rupture and geomorphologies resulting inaccurate mapping and location of faults and fault-pipe crossings. The results presented in this paper suggest the re-evaluation of design provisions in the current pipeline design guidelines to reduce the seismic risk of these geographically distributed structural systems.

1. INTRODUCTION

Buried continuous steel pipelines are commonly used for transporting oil and gas across the world. They generally cover long distances and their exposure to the earthquake threats while crossing seismically active faults cannot be overlooked at the design stage. Unlike water pipelines, which are generally constructed as segmented pipes, the continuous steel pipelines are more likely to suffer damage due to permanent fault displacements (PFDs) rather than ground strains caused by seismic wave propagation. The 1971 San Fernando, 1994 Northridge, 1999 Kocaeli and 2001 Alaska earthquakes caused serious continuous pipeline damages at fault crossings with human casualties and economic losses. Therefore, reliable seismic hazard and risk assessment of continuous pipelines at fault crossings is important to mobilize the

---

[1] Corresponding author: sinan.akkar@boun.edu.tr

most efficient design and retrofitting techniques for earthquake induced risk mitigation.

When a continuous pipeline is subjected to surface fault rupture, the resulting stresses along the pipeline are complicated because they depend on many factors such as style-of-faulting, pipe material, pipe dimensions (thickness and diameter), pipe alignment with respect to fault strike and soil property surrounding the pipe. There are numerous studies in the literature that investigate the mechanical behavior of a pipeline at fault crossings (e.g. [13-18]). The results of these studies do not consider the earthquake originated uncertainties that may affect the damage state in the continuous buried pipelines. The probabilistic seismic risk analysis of buried pipelines are focused on segmented pipelines (e.g. [1-6]) by using empirical fragility functions that relate ground shaking (e.g. [7-10]) or ground strain (e.g. [11-12]) to repair rate. (Geographically distributed segmented pipelines are vulnerable to transient ground shaking). Therefore, probabilistic failure due to fault crossings (i.e., PFDs) critical to continuous steel pipelines is yet to be investigated in sufficient details.

Recent developments in probabilistic PFD hazard [19-21], however, provide good basis to implement probabilistic seismic risk assessment to continuous pipelines. Understanding the probabilistic risk of pipelines at different earthquake levels would be important to the pipeline operator to take necessary actions for mitigating seismic pipeline vulnerability.

This study presents the theory and application of probabilistic seismic risk assessment of buried continuous steel pipelines induced by PFD. The probabilistic PFD is computed via Monte Carlo (MC) simulations and probabilistic risk is represented by the expected annual exceedance rate of pipeline failure. The paper first introduces the MC-based hazard assessment method (theory and application) to model probabilistic PFD. This is followed by the discussions on probabilistic risk assessment of pipeline failure triggered by PFD. The presented case studies facilitate the understanding of these concepts and also show the significance of uncertainties resulting from the intrinsic nature of earthquake process as well as pipeline mechanical behavior. The complexities in earthquake rupture are accounted for by mapping accuracy of faults and complexity of fault rupture that would results in variations in the relative locations of ruptured fault and pipe. The mechanical behavior of pipe is constrained to pipe cross-section dimension, soil properties surrounding the buried pipe, buried depth of pipe and variations in pipe-fault crossing angle. The observations from the presented case studies are discussed within the context of design and risk assessment regulations enforced by current continuous pipeline design guidelines.

2. METHODOLOGY

2.1 Monte-Carlo based probabilistic hazard for PFD

The current state-of-practice (e.g., pipeline designs codes) tends to estimate PFDs deterministically from empirical surface rupture vs. magnitude relationships (e.g. [22]). Alternative to this approach, Youngs et al. [20] developed the probabilistic fault displacement hazard assessment (PFDHA) for the Yucca Mountain Nuclear Waste Repository Project for normal faults to expresses the annual exceedance rates of fault displacements at different thresholds. The methodology is inspired from conventional probabilistic seismic hazard assessment (PSHA). It is further studied in Petersen et al. [21] for strike-slip faults by including the fault mapping accuracy and ruptured fault complexity. Our method uses the Petersen et al. model and it considers the likely occurrence of on-fault (*D*) and off-fault (*d*) displacements. The former displacement occurs on the major ruptured fault and the latter displacement typically represents discontinuous shear-failures at locations far from the principal fault.
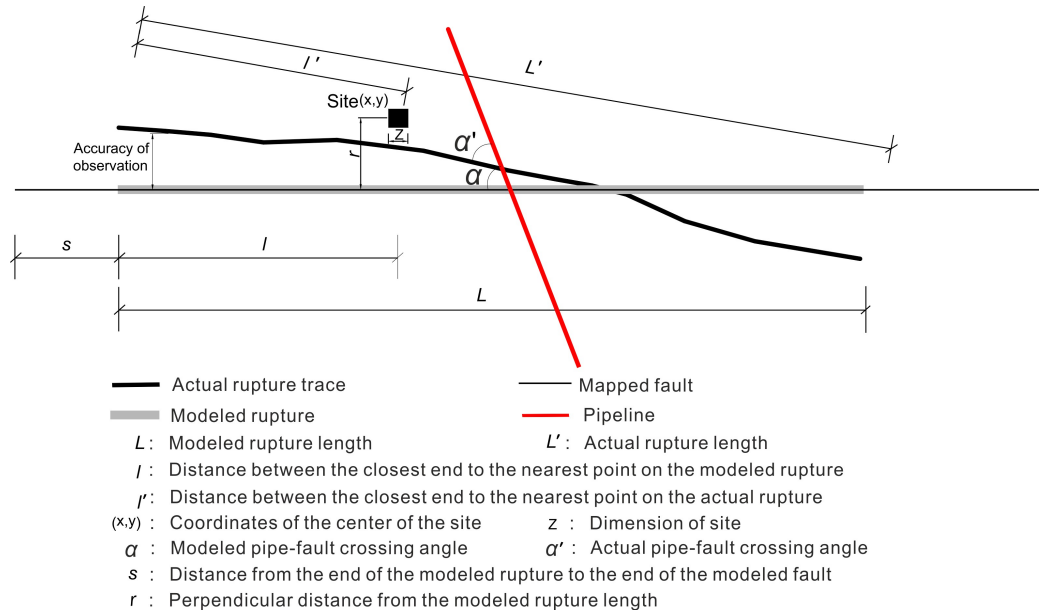

Figure 1. Modeled and actual fault layout of Petersen et al. [21] PFDHA approach for strike-slip earthquakes. The *accuracy of observation* represents the combined effects of fault mapping accuracy and rupture complexity on the *modeled* and *actual* rupture.

Our interpretations of ruptured fault segment and site geometry used in Petersen et al. [21] are presented in Figure 1. The variables on the figure are described in the legends and are used in Equations (1) and (2) that will be explained in the following paragraphs. The plot shows the *modeled* (*mapped*) and *actual* fault layout. The *modeled* configuration is used in PFDHA by incorporating the uncertainties due to fault mapping inaccuracy and complexity of fault rupture. Fault mapping accuracy is used to quantify how well the geological maps predict the location of actual fault by comparing the fault maps produced prior to an earthquake (mapped fault) to the

location of surface ruptures produced along that fault after the earthquake [21]. This phenomenon is, in fact, an epistemic uncertainty and Petersen et al. [21] quantify it by single- or two-sided sigma probability distribution of error distance from the mapped fault to the location of the actual surface rupture. The sigma in this distribution qualifies the mapping accuracy as accurate, approximate, concealed and inferred. Needless to say, the accurate fault mapping category is described by a small sigma whereas the inferred mapping accuracy refers to a very large uncertainty in the *modeled* (*mapped*) fault location. The fault complexity quantifies the complexities in fault geometry: splay faults, faults with strike changes or faults stepping over to a new trace are classified as complex faults. Petersen et al. [21] also quantify the fault complexity by a single- or two-sided probability distribution and larger sigma refers to a more complex classification. The definitions and associated sigma values of fault mapping accuracy and fault rupture complexity are given in Tables 2 and 3 of Petersen et al. [21]. We use these sigma values in our PFDHA to introduce offsets normal to the strike of the *mapped* (*modeled*) fault in order to represent the potential deviations in the *modeled* fault trace.

Equations (1) and (2) show the annual exceedance rates of on-fault $\gamma(D \geq D_0)$ and off-fault $\gamma(d \geq d_0)$ displacements that are given in Petersen et al. [21].

$$\gamma(D \geq D_0) = v_{\min} \int_{m,s} f_{M,S}(m,s) P[sr \neq 0|m] \int_r P[D \neq 0|z, sr \neq 0]$$
$$\times P[D \geq D_0|l/L, m, D \neq 0] f_{l/L}(l/L) f_R(r) d(l/L) dr dm ds \tag{1}$$

$$\gamma(d \geq d_0) = v_{\min} \int_{m,s} f_{M,S}(m,s) P[sr \neq 0|m] \int_r P[d \neq 0|r, z, sr \neq 0]$$
$$\times P[d \geq d_0|r, m, d \neq 0] f_R(r) dr dm ds \tag{2}$$

The probabilistic terms in Equation (1) include (a) the uncertainty in rupture location, r, due to random variation of rupture along the fault as well as the fault complexity and mapping inaccuracy, $f(r)$; (b) the joint probability to characterize the relation between earthquake magnitude (m) and rupture location (s), $f_{M,S}(m,s)$; (c) the probability of observing surface rupture (sr) conditioned on earthquake magnitude, $P(sr \neq 0|m)$; (d) given a nonzero surface rupture the probability of observing a nonzero on-fault displacement at a site of dimension z, $P(D \neq 0|z, sr \neq 0)$ and (e) the probability of on-fault displacement exceeding a threshold D_0 conditioned on rupture geometry and earthquake size. The last conditional probability is lognormal and is developed from an on-fault empirical displacement predictive model (on-fault displacement GMPE). The probability distribution $f_{l/L}(l/L)$ considers the uncertainty between the relative positions of rupture and site locations for on-fault displacements resulting from complexities in rupture process. Apart from these probabilistic terms, the minimum rate, v_{min}, constrains the frequency of earthquake occurrence in the model. It is a function of magnitude and can be a single rupture rate or can be a function of

cumulative earthquakes above a minimum magnitude of engineering significance (Youngs et al. [20]). As in the case of conventional PSHA, the upper and lower bounds of distance, rupture location and magnitude depend on the area covered in PFDHA as well as geologic (including dimension) and seismic activity information of seismic sources within that area. The judgement on the limits of l/L ratio can reflect levels in fault rupture complexity and fault mapping accuracy.

The probabilistic terms that describe the annual exceedance rate of off-fault displacements $\gamma(d \geq d_0)$ show some similarities with Equation (1). In fact, the first three probabilities defined in $\gamma(D \geq D_0)$ also exist in $\gamma(d \geq d_0)$. In the computation of $\gamma(d \geq d_0)$, the probability of nonzero off-fault displacement given a nonzero surface rupture $[P(d \neq 0|_{r, z, sr \neq 0})]$ not only depends on the size of the site (z) but also on the perpendicular distance, r, between the site and the rupture. This is because the discontinuous off-fault displacements are expected to occur away from the fault due to shears and fractures in the vicinity of principle rupture. The empirical GMPE to describe the probability of off-fault displacement exceeding a threshold d_0 $[P(d \geq d_0|_{r, m, d \neq 0})]$ is a function of r and m for $\gamma(d \geq d_0)$. The reader is referred to Petersen et al. [21] and Youngs et al. [20] for details of conventional probabilistic fault displacement hazard integral. The next paragraph explains the integration of these probabilities to MC-based PFD hazard.

Our MC-based PFD hazard assessment starts with the generation of synthetic earthquake catalogs to reflect the temporal seismicity of the subject fault. The procedure of generating synthetic catalogs is already given in Akkar and Cheng [23]. Each synthetic catalog contains a series of events that follows the designated magnitude recurrence model within the predefined catalog period. For each event in the synthetic catalog, Figure 2 shows the proposed procedure to generate probabilistic on-fault and off-fault displacements at the centroids of the cells covered by the region of interest. The grid size is z and it varies from 25 m to 200 m in Petersen et al. [21] to account for different levels of accuracy in rupture probability. The mesh gridding is done only within several hundred meters (e.g., 150 m) from each side of the fault because fault displacements decay rapidly with increasing distance from the ruptured fault segment.
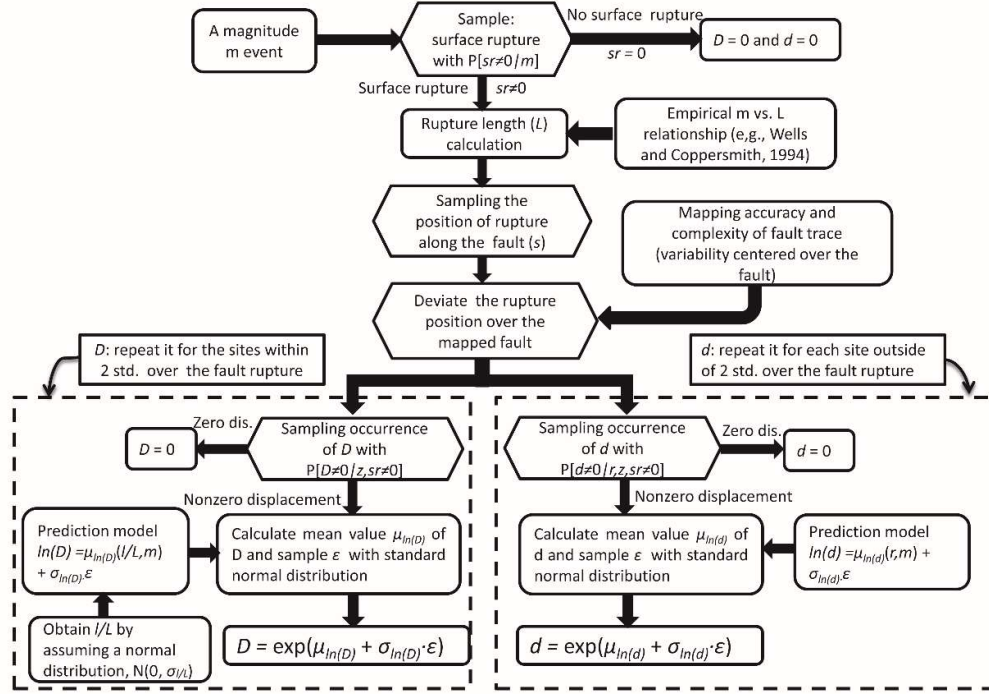
Figure 2. Proposed MC-based permanent fault displacement hazard assessment procedure

We first compute the conditional probability of observing surface rupture on the fault, $P(sr \neq 0|_m)$, for each scenario event with a designated magnitude m in the earthquake catalog (Equation (3)).

$$P(sr \neq 0|_m) = \frac{e^{(-1 .51+2.053m)}}{1+e^{(-12.51+2.053m)}} \tag{3}$$

The conditional probability follows Bernoulli distribution that samples the "success" ($sr \neq 0$) or "failure" ($sr = 0$) of a random event under the computed probability given in Equation (3). If Bernoulli distribution samples "failure", both on- and off-fault displacements are zero for that scenario event. If the earthquake with surface rupture is sampled, an empirical m vs. L scaling relationship is used (e.g. [22]) to determine the rupture length, L. The rupture position (s) is randomly placed along the entire fault assuming a uniform distribution. The likely deviation in the rupture location from the mapped fault trace due to mapping uncertainty is determined from a two-sided normal probability distribution proposed by Petersen et al. [21]. (See Table 2 in the referred article). After determining the final location of the ruptured segment, the on- and off-fault displacements are generated as given in the dashed boxes in Figure 2. The random generation of on- and off-fault displacements start with the consideration of probabilities $P(D \neq 0|_{z, sr \neq 0})$ and $P(d \neq 0|_{r, z, sr \neq 0})$. These probabilities are expressed as power functions and are given in a tabular format in Petersen et al. [21] for different grid sizes. They also follow Bernoulli distribution and if the Bernoulli distribution samples "failure" for any one of these probabilities, the corresponding fault

displacement is taken as zero. (In practice, $P(D \neq 0|_{z, sr \neq 0})$ can be taken as unity and Bernoulli distribution samples "success" whenever a non-zero surface rupture is generated). Otherwise, the on- and off-fault displacements are estimated from the proposed empirical GMPEs by Petersen et al. [21]. These expressions are given in Equations (4) and (5).

$$
\begin{aligned}
\ln(D) &= 1.7969m + 8.5206(l/L) - 10.2855 + \varepsilon\sigma_{ln(D)}; \quad \text{l/L} \leq (l/L)_0 \\
&= 1.7685m - 7.8962 + \varepsilon\sigma_{\ln(D)}; \qquad\qquad\qquad l/L \geq (l/L)_0
\end{aligned}
\tag{4}
$$

$$
\ln(d) = 1.4016m - 0.1671\ln(r) + \varepsilon\sigma_{ln(d)})
\tag{5}
$$

Note that the on-fault displacement (Equation 4) is a bilinear function and $(l/L)_0 = 0.11736\times(-0.0311m+2.3893)$ is the intersection point where the equation changes from the first branch to the second. $\sigma_{ln(D)}$ and $\sigma_{ln(d)}$ describe the logarithmic standard deviations associated with the on- and off-fault displacement GMPEs, respectively. ε designates the number of standard deviations above or below the logarithmic mean estimates. Consistent with the conventional wisdom in GMPEs, D and d are log-normal varieties whereas ε is normally distributed in the above expressions. Petersen et al. [21] propose three alternative prediction equations to estimate on-fault displacements depending on the observed data from the past strike-slip earthquakes. These equations are strictly valid for on-fault sites (cells) after considering the mapping uncertainty and fault complexity while determining the location of ruptured segment on the principal fault. We treat l/L as a normal variate to consider the uncertainty between the relative positions of rupture and site locations resulting from complexities in rupture process. The off-fault displacement predictive model is used at the sites (cells) encircling the major ruptured fault segment. The off-fault sites are only within few hundred meters from both sides of the ruptured fault segment due to rapid decay of fault displacements with distance.

The algorithm given in Figure 2 is repeated for all the earthquakes in the generated synthetic catalogs to compute the on- and off-fault displacement distributions at the centroid of each cell. The annual exceedance rates of on-fault and off-fault displacements at each cell for predefined threshold levels are determined from the following expressions:

$$
\lambda_j(D \geq D_0) = \frac{total\ number\ of\ D{\geq}D_0\ at\ site\ j}{total\ number\ of\ simulated\ earthquak\ \ catalogs\times catalog\ period}
\tag{6}
$$

$$
\lambda_j(d \geq d_0) = \frac{total\ number\ of\ d{\geq}d_0\ at\ site\ j}{total\ number\ of\ simulated\ earthquake\ catalogs\times catalog\ period}
\tag{7}
$$

In Equations (6) and (7) j refers to the cell index whereas D_0 and d_0 are the threshold on-fault and off-fault displacements, respectively. The on-fault and off-fault displacement hazard curves at cell j are obtained from the computation of $\lambda_j(D \geq D_0)$ and $\lambda_j(d \geq d_0)$ for a set of D_0 and d_0, respectively. The total permanent displacement

hazard curve at cell j is the sum of on- and off-fault hazard curves corresponding to cell j.

2.2 Probabilistic seismic risk assessment of pipelines due to PFD

The pipeline seismic risk against faults rupturing at the surface is represented by the annual exceedance rate of pipeline failure. This is achieved by integrating the probabilistic fault displacement hazard, mechanical response of pipe due to fault displacement and empirical pipe fragility function. The concept is similar to the conventional probabilistic seismic risk assessment [24] but we could have implemented the simulation-based risk assessment as well. Since both tensile and compressive strains developed along the pipe during an earthquake can cause pipe's failure, the seismic risk of pipe failure should consider the aggregated effects of these two strain components. The formula to calculate the seismic risk are given in Equations (8) and (9). Note that the indices i and j in the discrete form of Equation (8) stand for discretized fault displacements and pipe-fault crossing angles (α) ranging from 1 to n and 1 to m, respectively.

$$\lambda_{failure} = \int_D \int_\alpha P\big(F\big|\varepsilon(d,\alpha,\boldsymbol{\theta})\big)\, f_D(d) f_A(\alpha)\, d(d)\, d(\alpha) \tag{8}$$

$$= \sum_{i=1}^n \sum_{j=1}^m P\left(F\Big|\varepsilon\big(d_i,\alpha_j,\boldsymbol{\theta}\big)\right) \triangle (v_{d_i}) P(\alpha_j)$$

where ε stands for tensile strain, ε_t, or compressive strain, ε_c; and $P(F|\varepsilon)$ is calculated from the equation given below

$$P\big(F\big|\varepsilon(d,\alpha,\boldsymbol{\theta})\big) = 1 - \big\{1 - P\big(F_t|\varepsilon_t(d,\alpha,\boldsymbol{\theta})\big)\big\} \cdot \big\{1 - P\big(F_c|\varepsilon_c(d,\alpha,\boldsymbol{\theta})\big)\big\} \tag{9}$$

$$= P\big(F_t|\varepsilon_t(d,\alpha,\boldsymbol{\theta})\big) + P\big(F_c|\varepsilon_c(d,\alpha,\boldsymbol{\theta})\big) - P\big(F_t|\varepsilon_t(d,\alpha,\boldsymbol{\theta})\big) \cdot P\big(F_c|\varepsilon_c(d,\alpha,\boldsymbol{\theta})\big)$$

In the above equations, $\lambda_{failure}$ is total annual rate of pipeline failure at the fault crossing. The term $P(F|\varepsilon\,(d,\alpha,\boldsymbol{\theta})$ represents the probability of pipeline failure due to tensile (ε_t) or compressive (ε_c) strains developed along the pipe at the fault crossing. $P(F_t|\varepsilon_t(d,\alpha,\boldsymbol{\theta})$ and $P(F_c|\varepsilon_c(d,\alpha,\boldsymbol{\theta}))$ are the pipeline failure probabilities due to tensile strain (ε_t) and compressive strain (ε_c), respectively. The probability expressions in the risk integral represent pipe's fragility function for a certain level of pipe strain, ε, that varies with the fault displacement, d, and the fault-pipe crossing angle, α (Figure 1). The vector $\boldsymbol{\theta}$ in the fragility function describes the parameters (e.g., pipe buried depth, pipe diameter to thickness ratio and, D/t, etc.) that can affect pipe's seismic response. The probability distributions of fault displacement and fault-pipe crossing angle are represented by $f_D(d)$ and $f_A(\alpha)$. The probability distribution of α is characterized by truncated normal distribution. It maps the uncertainties in pipe-fault crossing angle due to fault rupture complexities and deficiencies in fault mapping

(variations from α to α' as shown in Figure 1). The fault displacement probability distribution, $f_D(d)$, shows the annual frequency of occurrence of the fault, d.

3. PERMANENT FAULT DISPLACEMENT HAZARD

We first discuss the significance of fault mapping accuracy on PFD. For this purpose, we used the case study in Petersen et al. [21] that also helped us to validate our MC-based PFD codes. The case study assumes a strike-slip fault with a characteristic magnitude of M_w 7 occurring, on average, every 140 years. Petersen et al. assume nonzero permanent fault displacement whenever there is a surface rupture on the fault [i.e., $P(D \neq 0|_{z, sr \neq 0}) = 1$]. They also adopt accurately mapped fault trace scenario in their example. We extended this scenario for approximate, concealed and inferred fault mapping uncertainties to account for morphological and geological complications along the actual fault trace. We ran the MC-based probabilistic fault displacement hazard by generating 40,000 simulations. Each simulation has an earthquake catalog period of 100-year. We considered a stripe of 150m from each side of the fault segment and computed the variation of PFD along the entire fault length at every 100m. The sizes of cells on each side of the fault segment are taken as 25m × 25m. The variation of permanent fault displacement is computed at every 1m within the 150m-stripe. For simplification, we disregarded the uncertainty in l/L due to random variations in fault rupture.

Figure 3.a shows the distribution of PFD along the fault trace for a 475-year return period when fault mapping is assumed to be accurate. The PFD is maximum on the ruptured fault trace and attenuates very rapidly as one moves away from the fault in the perpendicular direction. Figure 3.b presents the MC-based probabilistic permanent on-fault displacement at the center of the fault for accurate, approximate, concealed and inferred fault traces. The accurate fault mapping case compares our PFD computations with the results of Petersen et al. [21]. The variation in the displacement profile is given along the 150m stripe from each side of the fault. Our MC-based probabilistic approach yields very similar permanent displacements to those of Petersen et al. The variation of PFD changes as the level of mapping inaccuracy increases. The complex, concealed and inferred modeling of mapping accuracy introduce a considerable amount of uncertainty in the PFD distribution. This suggests that the ruptured fault segment can be shifted several tens of meters away from the mapped fault trace due to complications occurring in the actual rupture process.
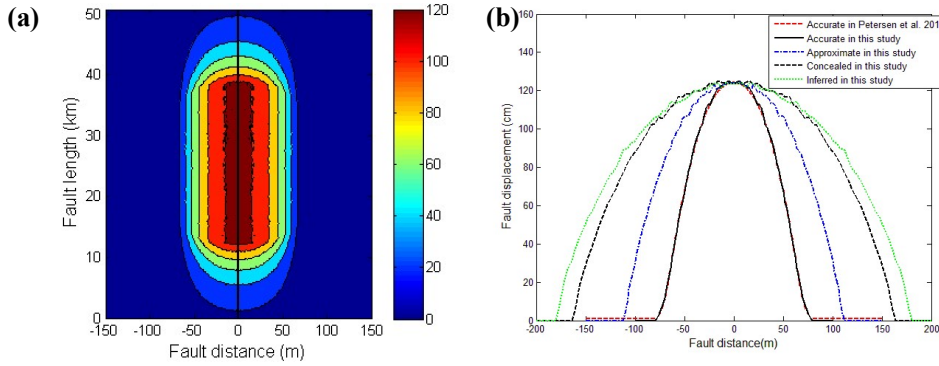
Figure 3. MC-based probabilistic PFD by adopting the case study in Petersen et al. (2011): (a) distribution of 475-year permanent fault displacement (accurate fault mapping) along the fault strike, (b) 475-year on-fault displacements at the center of the fault for different fault mapping accuracy levels. Mapping accuracies are represented by two-sided normal distributions with sigma values of 26.89m (accurate), 43.82m (approximate), concealed (65.52m), inferred (72.69m).

The next case presents the variation of on-fault PFDs along the fault segment by associating the uncertainty in l/L in PFDHA to consider the effects of complications between the relative positions of rupture and site. To make this example more relevant for continuous pipeline design and risk assessment, we assumed a fictitious pipeline crossing the fault segment at discrete locations along the fault with a certain pipe-fault crossing angle (Figure 4.a).Thus, we focus on on-fault PFD and each l/L represents a particular pipe-fault crossing. Given α (30° and 90° in this case study), we computed the annual exceedance rates along the fault segment ($0 \leq l/L \leq 1$) for on-fault PFDs that would yield 2% and 4% tensile strains at the pipe cross-section crossing the fault. The imposed tensile strains grossly represent normal operability (NOL, $\varepsilon = 2\%$) and pressure integrity (PIL, $\varepsilon = 4\%$) levels for butt-welded continuous pipelines (ALA, 2001). The NOL performance level refers to pipeline serviceability under frequent events whereas the later strain limit is used as an important condition to be satisfied under design level ground motions. We assumed accurate fault mapping associated with a hypothetical l/L uncertainty that is represented by a zero mean normal distribution with a standard deviation of $\sigma_{l/L} = 0.1$. Similar to the previous case study, we ran 40,000 MC simulations for a 100-year catalog period (i.e., 4,000,000 years of total catalog duration) for a strike-slip fault segment rupturing with characteristic magnitudes between M_w 7 and M_w 7.5 with an average slip rate of 20 mm/year.

The fictitious pipe-fault configuration and mean annual exceedance rates as a function of l/L and α are given in Figure 4. As depicted from this figure, the annual exceedance rates are very sensitive to variations in l/L and α. The exceedance rate of a particular on-fault PFD value that would render one of the above performance levels is low towards the fault edges and it is higher towards the center of the fault segment (maximum at $l/L = 0.5$). The increase in α generally results in lower annual exceedance rates. Since the required PFD for a certain strain level is inversely

proportional with PFD annual exceedance rate, steeper pipe-fault crossing angles and fault-crossings closer to the edges of ruptured fault segments would be more critical for seismic design and assessment of continuous pipelines. The uncertainty in l/L has little effect on the annual exceedance rates (or amplitude of PFDs). Currently, the seismic design of continuous pipelines is based on fixed mean annual exceedance rates (e.g. [25-26]) and disregard complexities stemming from fault rupture complexities. This case study as well as the previous one suggest that the current state-of-practice may yield non-uniform risk for continuous pipelines under earthquake induced hazard.
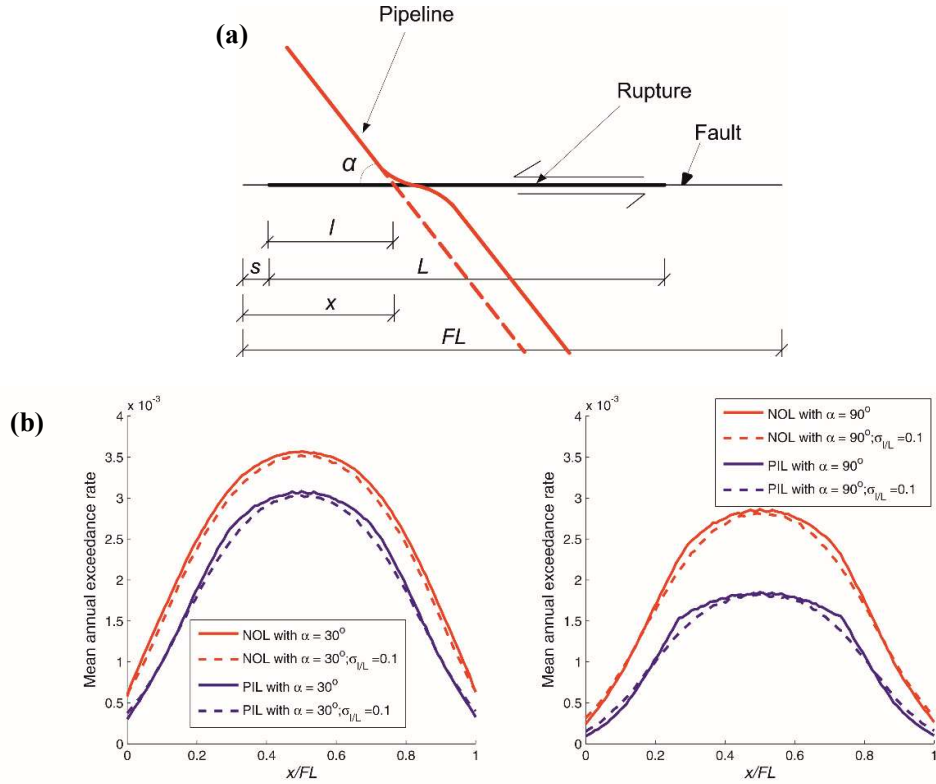

Figure 4. (a) Pipeline-fault layout: x denotes distance from the end of rupture to the pipe crossing location along the fault, α is the pipe-fault crossing angle, s is distance from the end of the rupture to the end of the fault, l is the length of ruptured fault segment and FL is the fault length; (b) Variation of mean annual exceedance rates as a function of pipe-fault crossing location and angle ($\alpha = 30°$ and $90°$) for 2% (Normal Operability Level) and 4% (Pressure Integrity Level) tensile strains. Dashed lines in mean annual exceedance rates display the cases when the uncertainty in l/L is considered.

4. PROBABILISTIC SEISMIC RISK DUE to PFD HAZARD

The previous section emphasizes the importance of PFD hazard and its modeling uncertainty under the influence of fault mapping accuracy and fault rupture

complexity resulting in variations in the relative positions of rupture and site. The implications of PFD hazard in seismic design and vulnerability of continuous pipelines are discussed in this section. We implement the probabilistic risk integral given in Equations (8) and (9).

The PFD hazard is represented by two strike-slip fault scenarios having (1) a slip rate of 15 mm/year with characteristic magnitudes distributed uniformly between M_w 7.0 and M_w 7.5 (Scenario 1) and (2) a slip rate of 20 mm/year with a uniform characteristic magnitude distribution between M_w 7.5 and M_w 8.0 (Scenario 2). Scenarios 1 and 2 can represent moderate-to-high seismicity in active fault zones (e.g., East Anatolian and North Anatolian faults). The uncertainties due to fault mapping are reflected on to the calculations by assuming *approximate* mapped fault accuracy conditions. The inaccuracy in α to acknowledge the intricate nature of fault rupture is mimicked by truncated normal distribution. We disregarded the uncertainty in l/L as its effect on PFD is limited (see Figure 4). We also assumed the pipe crossing the fault at the middle of the ruptured fault segment. Probabilistic PFD hazard is computed by running 40,000 MC simulations that use 100-year catalog interval in each run (a total of 4×10^6 years). This routine is implemented throughout this study as it would yield reliable PFD for annual exceedance rates up to 10^{-4}. The reader is referred to Akkar and Cheng [23] as well as references cited in that paper for a broader discussion on number of MC simulations vs. reliability of hazard estimations.

The cases studies consider continuous pipelines casted from S450 steel featuring an external diameter D of 36in (~0.91m) with four different wall thicknesses t, namely 1/4in (~6.4mm), 3/8in (~9.5mm), 1/2in. (~12.7mm) and 5/8 in (~15.9mm). Accordingly, the corresponding diameter-to-thickness ratios, *D/t,* are equal to 144, 96, 72, and 57.6, respectively. The considered material and pipe sizes cover a wide range of oil and gas transmitting continuous pipelines and would be helpful to generalize our discussions on pipeline seismic risk. The case studies in this section also consider four different buried pipe depths (i.e., 1m, 1.5m, 2m and 3m) to consider the effects of different types of soil conditions on the continuous pipeline risk.

Table 1. Key parameters and corresponding values for probabilistic continuous pipeline risk assessment due to PFD

Parameter	Considered values
Seismic activity	Characteristic earthquake recurrence model
	Scenario 1: M_w 7.0 - M_w 7.5, ṡ = 15 mm/year (EAF)
	Scenario 2: M_w 7.5 - M_w 8.0, ṡ = 20 mm/year (NAF)
Rupture location uncertainty	Fault-pipe crossing angles ranging between $10° \leq \alpha \leq 90°$
	having 2σ truncated Normal distribution with $\sigma = 2.5°$ and $5°$
Mapping accuracy	Two-sided normal distribution with $\sigma = 43.82$m
Ratio of pipe diameter to wall thickness (*D/t*)	144; 96; 72; and 57.6
Buried pipe depth	1m; 1.5m; 2m; and 3m
Soil conditions surrounding the buried pipes	Sand: friction angle=36°, cohesion= 0kPa
	Soft clay: friction angle=0°, cohesion= 50kPa
	Stiff clay: friction angle=0°, cohesion = 200kPa

Figure 5 shows a generic pipeline segment crossing a strike-slip fault. When the fault ruptures at the ground surface, the pipeline will be subjected to a deformation pattern as illustrated in this figure. It may suffer from large tensile and compressive strain levels at critical locations in the vicinity of fault-pipeline crossing. The deformations and therefore stresses can be beyond the elastic capacity of pipe material at such critical locations and may lead to abrupt failures. The following subsections first discuss the pipeline strain levels for a set of soil conditions and development of pipe fragilities for tensile and compressive strains. The rest of the section uses this information to compute probabilistic pipeline failure risk and major parameters contributing to this risk.
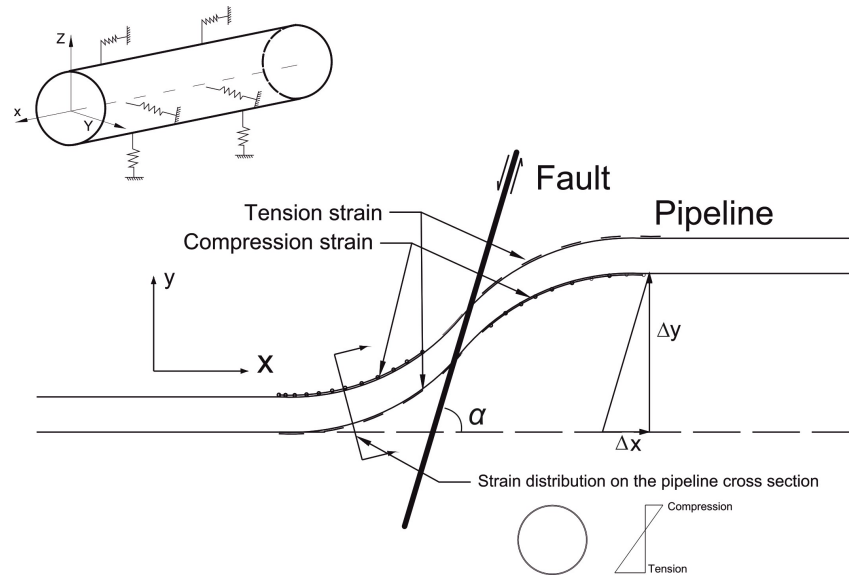

Figure 5. State of strains on the pipe section crossing a strike-slip fault. Dashed lines indicate tension surfaces whereas dotted lines represent compression. α is the fault-pipe crossing angle; Δx and Δy are the tangential and normal components of PFD causing tension and compression at the pipe cross-section. The horizontal and vertical springs and the representative 3D pipe on the upper left corner simulate soil-pipe interaction.

4.1 Pipeline strain states under different soil conditions and buried depths

We use the analytical method in Karamitros et al. [17] to calculate strains along the pipeline at the fault crossings. The steel type and pipe sizes for strain calculations are already presented in Table 1. The interaction between pipe and surrounding soil (mimicked either as dense sand, soft or stiff clay soils) is modeled with bilinear elastoplastic springs [9, 26]. The soil springs used in the analysis are recommended in ALA (2001; 2005) [9, 26] that are validated by Karamitros et al. [17] by a series of 3D nonlinear Finite Element numerical analysis. Nevertheless, one can use the soil-spring models suggested in [27] and [28] to understand the associated modeling

uncertainty in soil-pipeline interaction. We did not run such analysis in our study because our objective is to set a probabilistic framework for PFD hazard and associated risk in continuous steel pipelines.

The spring properties of each soil type that vary as a function of buried pipe depth (H) are presented in Table 2. The maximum axial force (Tu) on pipe is independent of depth for soft and stiff clays. However, it increases with depth if the pipeline is surrounded by dense sand. The lateral surcharge (Pu) on pipe increases with depth regardless of soil type. Table 2 also shows the assumed yield displacements for axial ($0.5\Delta_T$) and lateral ($0.5\Delta_P$) springs used in pipeline modeling. The dense sand, soft and stiff clay properties used in the computation of axial and lateral forces are listed on the last three lines of Table 1. According to ALA guidelines [9, 26] soil properties representative of the backfill should be used to compute axial soil spring force. Other soil spring forces (e.g., lateral surcharge) should generally be based on the native (existing) soil properties. In our case studies, we did not consider any backfill material and we assumed that native soil surround the pipe throughout the pipeline. Thus, for the sake of pipeline construction practice, our discussions would mostly be valid for trenchless pipeline construction and self-boring techniques.

Table 2. Soil spring properties [9, 26] corresponding soil parameters used in the case studies

Soil type	H (m)	Tu (kN/m)	$0.5\Delta_T$ (mm)	Pu (kN/m)	$0.5\Delta_P$ (mm)
Dense sand	1	18.2	2.5	159.3	29.1
	1.5	27.4	2.5	262	39.1
	2	36.5	2.5	378.3	49.15
	3	54.7	2.5	647.5	69.4
Soft clay	1	135.8	5	232	29.1
	1.5	135.8	5	258.7	39.1
	2	135.8	5	275.5	49.15
	3	135.8	5	295	69.4
Stiff clay	1	220.9	4	928.1	29.1
	1.5	220.9	4	1034.8	39.1
	2	220.9	4	1101.9	49.15
	3	220.9	4	1180	69.4

Figure 6 shows the depth dependent change in tensile and compressive strains at the fault crossing under Scenario 1 for $D/t = 96$. We used two pipe-fault crossing angles ($\alpha = 45°$ and $\alpha = 85°$) and disregarded the associated uncertainty in α for simplicity. The comparative plots indicate that the maximum compressive and tensile strains are sensitive to buried depth when pipeline is surrounded by dense sand. The compressive strains are higher when pipelines are surrounded by sand. On the other hand, pipelines surrounded by clay type soils seem to be more vulnerable to tensile strains. The change in pipe-fault crossing angle becomes more critical when pipes are under

compression. Note that compressive strain reduces after it reaches to its maximum in all cases. This is because the strain state in pipe's compression zone changes and tensile strain starts to govern for larger PFDs after maximum compressive strain is reached. Dashed line crossing at 1.25% compressive strain plots indicate the theoretical commencement of local wrinkling [29] although experimental results suggest smaller compressive strain levels for pipe wrinkling (1/3rd to 1/4th of the theoretical wrinkling strain). The tensile strains above 5% should be considered with caution in our computations. The Karamitros et al. [17] model tends to overestimate tensile and compressive strains at steep fault-pipe crossings because of inaccurate curvature calculations for large deformation demands. Thus, we opt not to use the results of Karamitros et al. [17] for large PFDs and very steep fault-pipe crossings ($\alpha \geq 80°$).
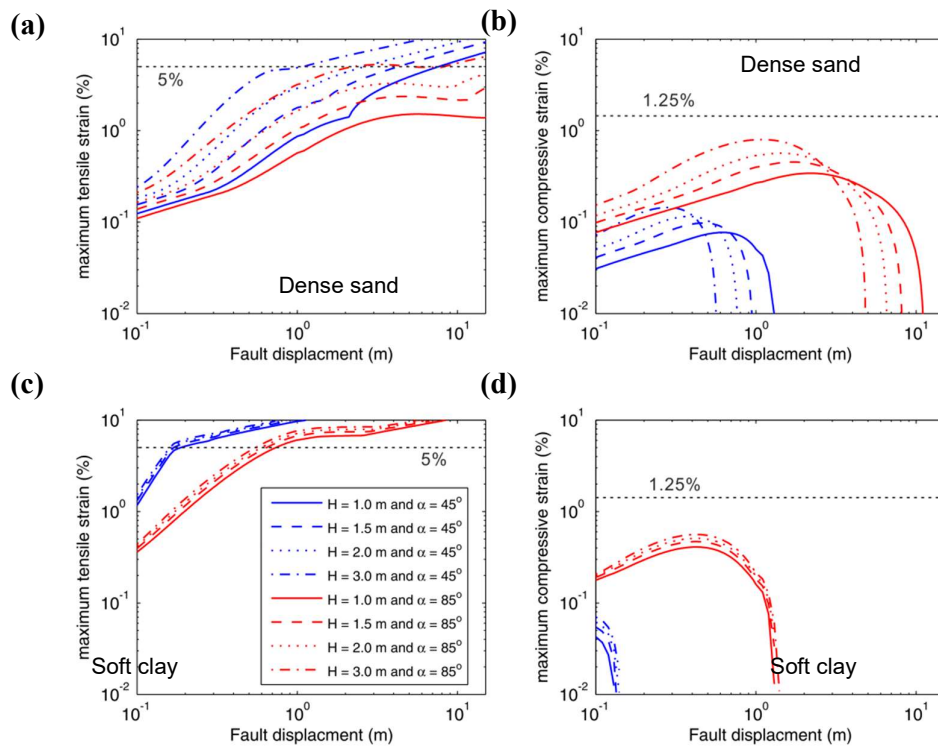

Figure 6. Maximum tensile and compressive pipe strains for a pipe of $D/t = 96$ at different bury depths (H) and pipe-fault crossing angles (α): (a) surrounded by dense sand and under tension, (b) surrounded by dense sand and under compression, (c) surrounded by soft clay and under tension and (d) surrounded by soft clay and compression

4.2 Pipe failure fragility

The continuous pipeline fragilities developed in this paper relate failure probability to different levels of tensile and compressive strains (i.e., P[failure|$\varepsilon(d,\alpha,\theta)$]). Assuming lognormal distribution, the failure fragilities are fitted over the data obtained from

literature survey. This is discussed in the subsequent paragraphs. We adopted minimization of the sum of squared errors method [30] for fitting fragility functions.

The tensile strains of 3% and 10% that correspond to 10% and 90% failure probability as suggested by Wijewickreme et al. [31] are used in the derivation of fragilities for tension failure. These deformation rates and corresponding failure probabilities are meaningful for steel pipelines with good-quality girth welds. The left tail (lower end) of lognormal tension fragility is constrained to yield no-failure at 1% tensile strain. The resulting fragility function is given in Figure 7.a.

The development of pipeline fragility for compressive stains is more complicated because failure probability due to compression is a function of D/t ratio. Wijewickreme et al. [31] assume that compressive strains corresponding to 10% and 90% failure probability are equal to $0.4/(D/t)$ and $2.4/(D/t)$, respectively. The theoretical commencement of local wrinkling (1.25% compressive strain) is in between $0.4/(D/t)$ and $2.4/(D/t)$. We used an additional constrain that assigns no-failure for compressive strains below $0.13/(D/t)$ to control the left tail of compression fragilities. The resulting fragility surface for pipeline failure due to compression is given in Figure 7.b for a set of D/t values. Table 3 lists the logarithmic means (θ) and standard deviations (B) of fitted lognormal failure fragilities for tension and compression. The ones for compression failure are presented for four D/t values that are developed in this study. These values will be used to calculate the probabilistic pipeline seismic risk in the following subsection.
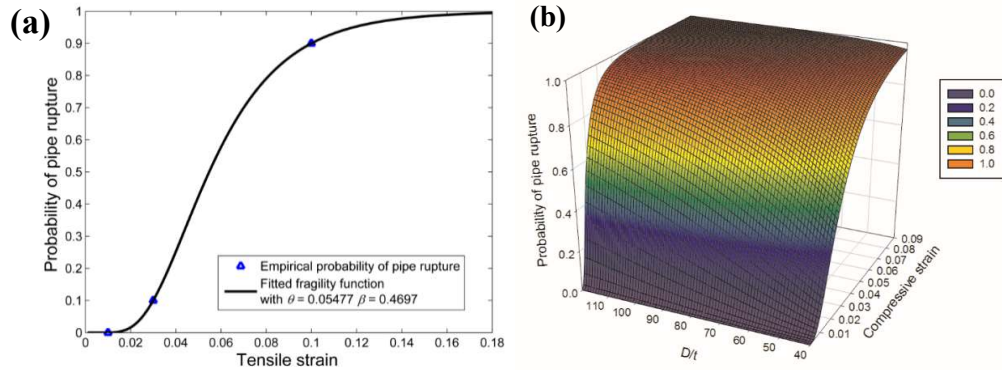

Figure 7. Pipeline fragility for (a) tension failure and (b) compression failure

Table 3. Logarithmic means and standard deviations of pipeline fragilities against tension and compression failures

Failure state	D/t	θ	B
Tension	-	0.05477	0.4697
Compression	57.6	0.0170	0.6987
Compression	72	0.0136	0.6987
Compression	96	0.0102	0.6987
Compression	144	0.0068	0.6987

4.3 Pipe failure risk

The first case study discusses the significance of pipe-fault crossing angles on pipeline risk. Earthquake scenario 1 is used to represent the seismic hazard. Figure 8 shows the annual failure rates (λ) for a pipeline buried at a depth of 1m under dense sand. The annual failure rates are computed for different α associated with the uncertainty in α to manifest the inherent complications during the fault rupture process. The inaccuracy in fault-pipe crossing angle is modeled by a truncated normal probability with alternative standard deviations of 2.5° and 5°. The plots display the results for two D/t ratios ($D/t = 57.6$ and D/$t = 72$) to emphasize the level of change in pipeline failure rates with changes in pipeline dimensions. The tensile strain is constrained to 5% to acknowledge modeling limitations in Karamitros et al. [17]. (See discussions on the limitations of Karamitros et al. [17] analysis method in the previous sections). The comparative plots show smaller failure rates (i.e., lesser probability of failure) with increasing α for pipe-fault crossing angles up to ~ 75°. This trend reverses and pipelines are exposed to higher failure probability for $\alpha > \sim$ 70°-75°. As discussed in the previous section, the reversed trend in pipeline failure probability towards larger α may be the result of over conservative computation of curvature that affects the accuracy of tensile and compressive pipe strains. To this end, the computed pipe failure rates of α greater than approximately 70°-75° may have serious limitations and should be evaluated with some caution. We also note that the mere consideration of tensile failure would underestimate the pipe failure risk towards larger pipe-fault crossing angle. This observation is in line with our assertion about the simultaneous consideration of tensile and compression strains in failure risk assessment of continuous pipelines. Needless to say, larger pipe dimensions reduce the pipe failure probability. Consideration of uncertainty in pipe-fault crossing angle icresaes the pipe failure probability towards large α values.
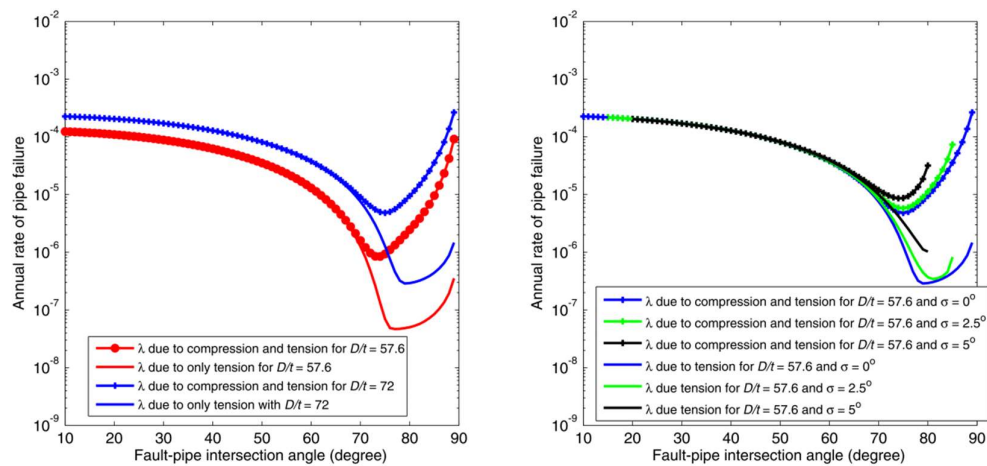
Figure 8. Annual failure rates of pipelines in terms of pipe-fault crossing angles and the effect of pipe dimensions and uncertainty in pipe-fault crossing angle on pipe failure risk.

Figure 9 displays the annual pipe failure rates under Scenario 1 and 2 earthquakes for a fault-pipe crossing angle of 60° and a pipe buried depth of 1m under different soil conditions. Therefore, this case study discusses the effects of soil as well as earthquake activity on the seismic vulnerability of continuous pipelines. The pipeline section is represented by $D/t = 57.6$ in the analysis. The presented annual failure rates advocate that pipelines surrounded by stiff clays run larger failure risks with respect to soft clay and sandy soils. The pipe failure probability is inherently higher under the second earthquake scenario although earthquake Scenario 1 would also lead to a serious pipeline failure risk regardless of soil type surrounding the pipeline. To this end, seismic activity after a certain level in earthquake prone regions would always yield high risk in continuous pipeline failure under PFD demand. In passing, we note that the fictitious pipeline discussed in Figure 9 would be exposed to higher pipe failure risk for larger pipeline buried depths. This is shown in Figure 10 that displays the variation of pipe failure rate in terms of pipe buried depth when seismic hazard is represented by earthquake Scenario 1. The pipe cross-section is the same as the one used in Figure 9.
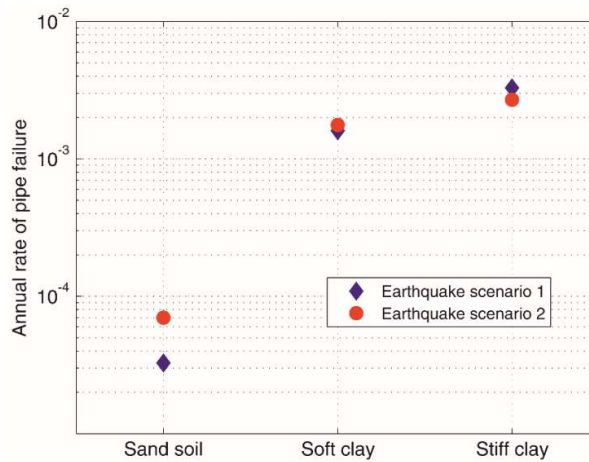

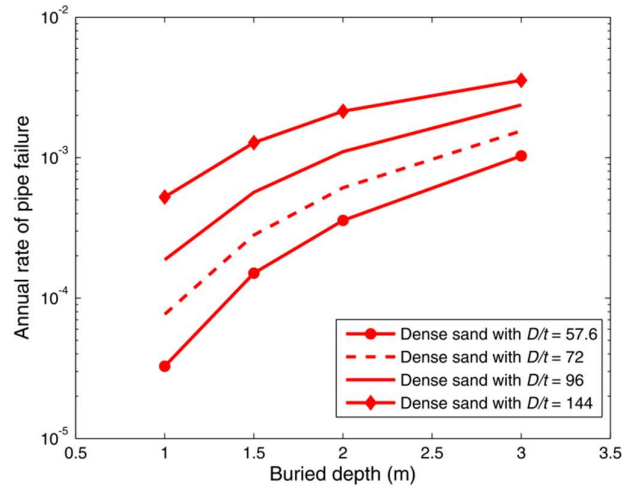Figure 9. Effect of soil type and earthquake activity on pipeline failure risk.

Figure 10. Variation of pipeline failure risk as a function of pipe buried depth. The results are developed for earthquake Scenario 1 under several D/t values used throughout the paper.

5. CONCLUSION

This paper discuses probabilistic hazard and risk assessment of continuous pipelines for PFD. The probabilistic PFD hazard has already been discussed in the literature but, to our knowledge, the probabilistic continuous pipeline risk is discussed to this extent for the first time. We used MC simulations for the probabilistic PFD hazard to account for uncertainties resulting from fault mapping accuracy and fault rupture complexity. The probabilistic risk is computed through discretized risk integral and accounts for the uncertainty in fault-pipe crossing angle due to intrinsic complexities taking place during rupture process.

The illustrated case studies consider strike-slip fault rupture but the proposed framework can equally be applicable to PFD hazard and associated probabilistic risk triggered by normal, reverse or oblique ruptures. Integration of other fault displacement models (e.g., [19] for normal SoF and [32] for reverse SoF, etc.) and use of analytical (e.g., [16]) or finite element pipe analysis procedures would suffice to extend the discussions in the paper to a broader perspective. The discussions in the paper are limited to soil-pipeline modeling recommended by some of the well-known pipe guidelines [9, 26]. Enhanced soil spring models and effects of other mechanical features between soil and pipe interaction can enrich the presented discussions that can be the topic of a separate article. Our basic objective in the paper is to use a probabilistic framework in terms of hazard and risk for calling the attention of pipe design guidelines to some important factors that can be significant for pipe design under earthquake thread.

The probabilistic PFD hazard results of this study emphasize the significance of pipe-fault crossing location, the corresponding angle as well as complexities arising from earthquake process. These phenomena are currently addressed by ad-hoc deterministic approaches in the pipeline design codes with the implementation of empirical expressions that estimate an average PFD for a particular magnitude. Our probabilistic pipeline risk case studies also advocate the difficulty in deterministic assessment of failure in continuous pipelines as it depends on the cumulative effects of variations in pipe-fault crossing angle and associated uncertainties stemming from fault rupture, pipeline buried depth and soil conditions surrounding the pipeline. These complexities together with the uncertainties in PFD hazard may result in a non-uniform risk for pipelines designed in accordance with the current pipeline design provisions. In essence, they may fail to comply with the desired performance level under seismic actions. The performance-based earthquake design in current building codes have started to define risk-targeted earthquake demands and provide performance targets in accordance with the risk-targeted demand levels [33-34]. Such a rational can also be adopted for pipeline design and discussions in this paper partially address how this objective can be achieved.

ACKNOWLEDGEMENT

REFERENCES

1. McGuire RK, Seismic risk to lifeline systems: critical variables and sensitivities. Proceedings of 9th World Conference on Earthquake Engineering: Tokyo-kyoto, Japan, 1988.
2. Mashaly E-SA and Datta TK. Seismic risk analysis of buried pipelines. *Journal of transportation engineering* 1989; **115**(3): 232-52.
3. Pineda-Porras OA, Ordaz M. Seismic Damage Estimation in Buried Pipelines Due to Future Earthquakes-The Case of the Mexico City Water System. Earthquake-Resistant Structures-Design, Assessment and Rehabilitation-Chapter 5. INTECH Open Access Publisher; 2012.
4. Omidvar B, Eskandari M, Peyghaleh E. Seismic damage to urban areas due to failed buried fuel pipelines case study: fire following earthquake in the city of Kermanshah, Iran. *Natural Hazards* 2013; **67**(2):169-92.

5. Esposito S, d'Onofrio A, Santo A, Cavalieri F, Franchin P. Simulation‐Based Seismic Risk Assessment of Gas Distribution Networks. *Computer-Aided Civil and Infrastructure Engineering* 2015; **30**(7): 508-523.
6. Mousavi M, Hesari M, Azarbakht A. Seismic risk assessment of the 3rd Azerbaijan gas pipeline in Iran. *Natural Hazards* 2014; **74**(3):1327-48.
7. Katayama T, Kubo K, Sato N. Earthquake Damage to Water and Gas Distribution Systems, Proceedings of the U.S. National Conference on Earthquake Engineering: Oakland, 1975.
8. O'Rourke T, Jeon S. Factors Affecting the Earthquake Damage of Water Distribution Systems, Proceedings 5th U.S. Conference on Lifeline Earthquake Engineering: Seattle, 1999.
9. American Lifelines Alliance (ALA). Seismic Fragility Formulations for Water Systems, Part 1–Guideline, 2001.
10. FEMA (Federal Emergency Management Agency). Multi-hazard loss estimation methodology-earthquake model: HAZUS MR4 technical manual, Washington DC, 2004.
11. O'Rourke M. Analytical Fragility Relations for Buried Segmented Pipe," Proc. of TCLEE 2009, Lifeline Earthquake Engineering in a Multihazard Environment: Oakland, 2009.
12. O'Rourke M, Filipov E, Uçkan E. Towards Robust Fragility Relations for Buried Segmented Pipe in Ground Strain Areas. *Earthquake Spectra* 2014; doi: http://dx.doi.org/10.1193/032311EQS076M,
13. Datta TK. Seismic response of buried pipelines: a state-of-the-art review. *Nuclear Engineering and Design* 1999; **192**(2-3): 271-284.
14. Vazouras P, Karamanos SA, Dakoulas P. Finite element analysis of buried steel pipelines under strike-slip fault displacements. *Soil Dynamics and Earthquake Engineering* 2010; **30**(11):1361–76.
15. Vazouras P, Karamanos SA, Dakoulas P. Mechanical behavior of buried steel pipes crossing active strike-slip faults. Soil Dynamics and Earthquake Engineering. 2012; **41**:164-80.
16. Karamitros DK, Bouckovalas GD, Kouretzis GP, Gkesouli V. An analytical method for strength verification of buried steel pipelines at normal fault crossings. *Soil Dynamics and Earthquake Engineering* 2011; **31**(11): 1452-1464.
17. Karamitros DK, Bouckovalas GD, Kouretzis GP. Stress analysis of buried steel pipelines at strike-slip fault crossings. *Soil Dynamics and Earthquake Engineering* 2007; **27**(3): 200-211.
18. Uckan E, Akbas B, Shen J, Rou W, Paolacci F, O'Rourke M. A simplified analysis model for determining the seismic response of buried steel pipes at strike-slip fault crossings. *Soil Dynamics and Earthquake Engineering* 2015; **75**:55-65.
19. Stepp JC, Wong I, Whitney J, Quittmeyer R, Abrahamson N, Toro G, Youngs R, Coppersmith K, Savy J, Sullivan T, Yucca Mountain PSHA Project Members. Probabilistic seismic hazard analyses for ground motions and fault displacement at Yucca Mountain, Nevada. *Earthquake Spectra* 2001; **17**:113–150.
20. Youngs RR, Arabasz WJ, Anderson RE, Ramelli AR, Ake JP, Slemmons DB, et al. A methodology for probabilistic fault displacement hazard analysis (PFDHA). *Earthquake Spectra* 2003; **19**(1):191-219.
21. Petersen MD, Dawson TE, Chen R, Cao T, Wills CJ, Schwartz DP, Frankel AD. Fault displacement hazard for strike-slip faults. *Bulletin of the Seismological Society of America* 2011; **101**(2): 805-825.
22. Wells DL, Coppersmith KJ. New empirical relationships among magnitude, rupture length, rupture width, rupture area, and surface displacement. *Bulletin of the Seismological Society of America* 1994; **84**(4): 974–1002.

23. Akkar S, Cheng, Y. Application of a Monte‑Carlo simulation approach for the probabilistic assessment of seismic hazard for geographically distributed portfolio. *Earthquake Engineering and Structural Dynamics* 2015; **45**(4): 525–541.

24. McGuire RK. Seismic Hazard and Risk Analysis, Earthquake Engineering Research Institute: Oakland, CA, 2004.

25. IITK-GSDMA. Guidelines for seismic design of buried pipelines. Kanpur, India: Indian Institute of Technology. 2007.

26. American Lifeline Alliance (ALA). Design Guidelines for Seismic Resistant Water Pipeline Installations. Report FEMA, NIBS and ALA 2005/03. G&E Engineering Systems Inc, 2005.

27. Xie X, Symans MD, O'Rourke MJ, Abdoun TH, O'Rourke TD, Palmer MC, et al. Numerical modeling of buried HDPE pipelines subjected to normal faulting: a case study. Earthquake Spectra 2013; **29**(2):609–32.

28. Gas and Liquid Hydrocarbon Pipelines. Pipeline Research Council International (PRCI), Arlington, Virginia, Catalogue L51927, 2004.

29. ASCE. Guidelines for the Seismic Design of Oil and Gas Pipeline Systems. Committee on Gas and Liquid Fuel Lifeline, ASCE, 1984.

30. Baker JW. Efficient Analytical Fragility Function Fitting Using Dynamic Structural Analysis. *Earthquake Spectra* 2015; **31**(1):579-99.

31. Wijewickreme D, Honegger D, Mitchell A, Fitzell T. Seismic vulnerability assessment and retrofit of a major natural gas pipeline system: A case history. *Earthquake Spectra* 2005; **21**(2):539-67.

32. Moss ES, Ross ZE. Probabilistic fault displacement hazard analysis for reverse faults, *Bulletin of the Seismological Society of America* 2011; **101**(4):1542-53

33. Luco N, Ellingwood BR, Hamburger RO, Hooper JD, Kimball JK, Kircher CA. Risk-Targeted versus Current Seismic Design Maps for the Conterminous United States. Proceedings of the Structural Engineers Association of California 76th Annual Convention: Squaw Creek, 2007

34. Luco N, Gerstenberger MC, Uma SR, Ryu H, Liel AB, Raghunandan M. A methodology for post-mainshock probabilistic assessment of building collapse risk. Proceedings of the Ninth Pacific Conference on Earthquake Engineering Building an Earthquake-Resilient Society: Auckland, New Zealand, 2011.